Ukrainian Journal of Physical Optics
ISSUE 4
2026

Quiescent Vector Optical Solitons with Nonlinear Dispersion

Ahmed H. Arnous [1,2], Muhammad Amin S. Murad [3], Yakup Yildirim [4,5] & Anjan Biswas [6,7,8,9,10*]

[1] Department of Mathematical Sciences, Saveetha School of Engineering, SIMATS Chennai–602105, Tamilnadu, India
[2] Jadara Research Center, Jadara University, Irbid 21110, Jordan
[3] Department of Mathematics, College of Science, University of Duhok, Duhok, Iraq
[4] Department of Computer Engineering, Biruni University, Istanbul–34010, Turkey
[5] Mathematics Research Center, Near East University, 99138 Nicosia, Cyprus
[6] Department of Mathematics & Physics, Grambling State University, Grambling, LA 71245–2715, USA
[7] Department of Mathematics, Faculty of Science, Karadeniz Technical University, Trabzon–61080, Türkiye
[8] Department of Physics and Electronics, Khazar University, Baku AZ–1096, Azerbaijan
[9] Applied Science Research Center, Applied Science Private University, Amman–11937, Jordan
[10] Department of Mathematics and Applied Mathematics, Sefako Makgatho Health Sciences University, Medunsa–0204, South Africa
* Corresponding author: biswas.anjan@gmail.com

Received: 23.07.2026

Abstract. This paper investigates proportional vector quiescent solitons for a coupled nonlinear Schrödinger system with Kerr-type self-phase modulation, cross-phase modulation, and nonlinear dispersion. A proportional-amplitude reduction is introduced by assuming that the two components share a common envelope and phase while their relative amplitude remains fixed. Physically, this reduction selects an amplitude- and phase-locked vector mode with a fixed component intensity ratio. The reduction is admissible only when explicit algebraic compatibility relations connect the self-phase modulation, cross-phase modulation, and nonlinear dispersive coefficients. Under these constraints, the coupled model reduces to a scalar nonlinear Schrödinger equation with effective nonlinear dispersion. Within the proportional real-profile reduction, the nonlinear dispersive structure excludes nonzero-velocity localized waves and yields quiescent profiles. This zero-velocity conclusion is restricted to the common real-profile, constant-ratio, linear-phase ansatz and does not exclude moving waves with more general complex or nonproportional structures. The resulting stationary profile equation is solved by the enhanced direct algebraic method. Exact proportional vector quiescent wave families are obtained, including bright, kink-type, singular, Jacobi elliptic, Weierstrass elliptic, and straddled solutions. The limiting transitions among these families and the direct validation of the constructed profiles confirm the consistency of the analytical results. The full four-component perturbation operator is also derived. For a representative regular bright state, Chebyshev spectral computation places the spectrum on the imaginary axis to numerical tolerance, while direct Fourier–ETDRK4 propagation under independent component perturbations preserves the localized shape and vector locking over the simulated interval. These tests support numerical spectral stability and finite-time robustness for the tested bright branch only.

Keywords: vector quiescent solitons, coupled nonlinear Schrödinger system, nonlinear dispersion, quiescent reduction, spectral stability, perturbation robustness
UDC: 535.3
DOI: 10.3116/16091833/Ukr.J.Phys.Opt.2026.04054

1. Introduction

Nonlinear Schrödinger-type equations constitute one of the standard mathematical frameworks for dispersive nonlinear wave propagation in optical fibers, nonlinear media, and coherent wave systems. In their classical scalar cubic form, these models describe the balance between linear chromatic dispersion and Kerr self-phase modulation. This balance is responsible for the formation of localized optical pulses whose dispersion-induced spreading is compensated by nonlinear phase modulation. In many physical and mathematical settings, however, a scalar description is not sufficient because the optical field may involve two interacting components, two polarization states, two cores, or two coupled propagation channels. Coupled nonlinear Schrödinger systems therefore provide a natural extension of the scalar theory and allow self-phase modulation, cross-phase modulation, and vector coupling to be incorporated in a unified model.

The study of exact solutions for coupled nonlinear Schrödinger equations remains important because closed-form structures provide explicit benchmarks for the qualitative behavior of nonlinear dispersive systems. Recent investigations have reported periodic waves, optical solitons, fractional optical-fiber dynamics, stochastic Manakov solitons, Kundu–Mukherjee–Naskar solitons, and nonlinear optical pulses through several analytical schemes [1-5]. Highly dispersive optical solitons, dispersion-compensation mechanisms, higher-order nonlinear Schrödinger models, cubic–quartic optical solitons, stochastic dispersive solitons, and conservation laws for dispersive optical systems have also been reported [6-11]. These contributions show that changes in the dispersive structure, nonlinear law, or coupling mechanism may significantly modify the admissible localized waves.

Quiescent and stationary optical solitons form a special subclass of localized waves. In such solutions, the envelope is not transported as a moving pulse; instead, the spatial profile remains fixed, and the temporal evolution is carried by a phase factor. This distinguishes quiescent structures from ordinary traveling solitons with nonzero velocity [12, 13]. Quiescent profiles have appeared in nonlinear optical models involving quadratic–cubic nonlinearities, nonlinear chromatic dispersion, Kudryashov-type refractive-index laws, and generalized nonlinear Schrödinger equations with nonlinear dispersion [14-21]. Related stationary waves have also been studied in dissipative systems, Bragg-grating models, and complex Ginzburg–Landau optical equations [22-24]. These works indicate that nonlinear dispersive mechanisms may obstruct the usual traveling-wave balance and force localized real-profile waves into a pinned or quiescent regime.

The present work follows this viewpoint and considers a coupled nonlinear Schrödinger system in which nonlinear dispersion appears through amplitude-dependent dispersive corrections. To avoid relying on a narrowly specific material interpretation, these terms are referred to throughout this paper as nonlinear dispersion. Mathematically, they modify the dispersive part of the model through the products $|q|^2 q_{xx}$ and $|r|^2 r_{xx}$ and through the curvature-type corrections $(|q|^2)_{xx} q$ and $(|r|^2)_{xx} r$. This terminology emphasizes the structural role of these terms in the nonlinear wave equation rather than assigning them to a particular laser, waveguide, or optoelectronic platform.

Motivated by these developments, this work considers the coupled nonlinear Schrödinger system with nonlinear dispersion

$$iq_t + \alpha q_{xx} + \left(\beta_1 |q|^2 + \gamma_1 |r|^2\right) q + \delta_1 |q|^2 q_{xx} + \mu_1 \left(|q|^2\right)_{xx} q = 0, \tag{1}$$

$$ir_t + \alpha r_{xx} + \left(\beta_2 |r|^2 + \gamma_2 |q|^2\right) r + \delta_2 |r|^2 r_{xx} + \mu_2 \left(|r|^2\right)_{xx} r = 0, \tag{2}$$

where $q = q(x,t)$ and $r = r(x,t)$ are complex field components. The coefficient α represents the common linear chromatic dispersion. The parameters β_1 and β_2 describe self-phase modulation, whereas γ_1 and γ_2 describe cross-phase modulation. The coefficients δ_1 and δ_2 multiply the nonlinear dispersion terms, while μ_1 and μ_2 multiply the nonlinear dispersive curvature corrections.

The purpose of this paper is to construct vector quiescent solitons of (1)–(2). The analysis is based on proportional vector states, where the two components share the same spatial profile and phase but differ by a constant amplitude ratio. This reduction is not automatic; it requires explicit compatibility relations among the self-phase modulation, cross-phase modulation, and nonlinear dispersive coefficients. Once these relations are imposed, the coupled system reduces to a scalar nonlinear Schrödinger equation with nonlinear dispersion. The quiescent reduction and exact solution construction can then be performed systematically.

A proportional vector state cannot be obtained by merely duplicating a previously known scalar quiescent profile. Substitution of $r = \rho q$ into the two original field equations produces two scalar branches that are generally inequivalent. A common profile solves both equations only when the effective Kerr coefficients and both nonlinear-dispersive coefficients coincide, which yields the independent compatibility relations derived below. These relations determine the admissible component intensity ratio and restrict the original parameters to a specific coefficient manifold. Thus, the novelty is the identification and classification of the physically interpretable vector embedding of scalar-type quiescent profiles, together with its coefficient constraints and power partition, rather than a claim that every scalar functional form is new. Outside this compatibility manifold, a scalar quiescent solution cannot be lifted to a proportional solution of the coupled system.

The main contributions are as follows. First, the coefficient manifold supporting amplitude- and phase-locked vector states is derived, and the admissible ratio ρ is shown to determine the component power partition. Second, the physical interpretation of the proportional state is connected to polarization-locked or matched modal configurations, while the limits of a generic dual-core interpretation are stated. Third, the quiescent-wave constraint is derived for nonconstant localized profiles within the common real-envelope and linear-phase ansatz, without asserting nonexistence of more general moving vector waves. Fourth, the enhanced direct algebraic method is used to classify bright, kink-type, singular, Jacobi elliptic, Weierstrass elliptic, and straddled vector families and their limiting relations. Fifth, analytical residual verification establishes exactness, after which the full four-component linearized operator is derived for independent component perturbations. Sixth, a representative regular bright state is examined by Chebyshev spectral collocation and direct Fourier–ETDRK4 evolution, providing an explicit numerical test of spectral stability and finite-time perturbation robustness.

Section 5.3 distinguishes exactness from stability and addresses the latter without constraining perturbations to the proportional manifold. Independent disturbances of the two complex fields generate a four-component, variable-coefficient spectral problem containing both scalar-like and component-unlocking channels. The point and essential spectra are examined for a representative regular bright state, and the spectral conclusion is checked by direct propagation with independent amplitude and phase perturbations. The stability conclusion is deliberately restricted to the tested bright parameter set; no corresponding claim is made for the kink, elliptic, straddled, or singular families.

The main contributions are as follows. First, the proportional-amplitude reduction is derived, and its algebraic compatibility conditions are stated. Second, the quiescent-wave constraint is obtained for nonconstant localized real profiles. Third, the enhanced direct algebraic method is used to construct exact vector quiescent wave families, including bright, kink-type, singular, Jacobi elliptic, Weierstrass elliptic, and straddled solutions. Fourth, the limiting relations connecting the elliptic and straddled families with the standard hyperbolic solitons are clarified. Fifth, a validation section is included to verify that the constructed profiles satisfy the reduced stationary equation and, through the proportionality constraints, solve the original coupled system.

2. Proportional vector reduction and quiescent constraint

The proportional vector reduction is introduced to identify amplitude-locked two-component states of the coupled system. In this setting, the two fields share the same spatial profile and phase, while their relative amplitude is fixed by a constant real parameter. This assumption is not an arbitrary simplification; rather, it selects a consistent class of amplitude-locked vector states for which the coupled system can be reduced to a single scalar nonlinear Schrödinger -type equation. The reduction is admissible only when the two scalar branches generated from the original coupled equations coincide, which leads to explicit algebraic compatibility conditions among the self-phase modulation, cross-phase modulation, and nonlinear dispersive coefficients.

We seek proportional vector states in the form

$$r(x,t)=\rho q(x,t), \qquad \rho \neq 0, \tag{3}$$

where ρ is a real proportionality parameter. The relation $r=\rho q$ describes an amplitude- and phase-locked two-component state. The fields have the same envelope and carrier phase, while their pointwise intensity ratio is fixed according to

$$\frac{|r(x,t)|^2}{|q(x,t)|^2}=\rho^2. \tag{4}$$

Because ρ is real, the present reduction selects the in-phase or out-of-phase locked subclasses, corresponding to relative phase 0 or π. In an optical setting, this state may represent a polarization-locked mode in a weakly birefringent fiber when the group-velocity walk-off is negligible, and the two polarization components have matched linear dispersion. It may also represent two degenerate spatial or modal channels whose envelopes remain locked. Equations (1)–(2), however, contain cross-phase modulation but no explicit linear coupling terms such as Kr and Kq. They therefore do not directly describe a generic dual-core directional coupler. A dual-core interpretation is appropriate only after projection onto a locked symmetric or antisymmetric supermode, or in a regime where one such supermode is dynamically isolated. Substitution of (3) into (1) gives

$$iq_t+\alpha q_{xx}+(\beta_1+\gamma_1\rho^2)|q|^2 q+\delta_1|q|^2 q_{xx}+\mu_1(|q|^2)_{xx}q=0. \tag{5}$$

Similarly, substitution into (2) and division by ρ gives

$$iq_t+\alpha q_{xx}+(\gamma_2+\beta_2\rho^2)|q|^2 q+\delta_2\rho^2|q|^2 q_{xx}+\mu_2\rho^2(|q|^2)_{xx}q=0. \tag{6}$$

Therefore, the proportional reduction is consistent only if the two scalar branches coincide. This requires

$$\beta_1+\gamma_1\rho^2=\gamma_2+\beta_2\rho^2, \qquad \delta_1=\delta_2\rho^2, \qquad \mu_1=\mu_2\rho^2. \tag{7}$$

In the non-degenerate case $\gamma_1 \neq \beta_2$, $\delta_2 \neq 0$, and $\mu_2 \neq 0$, these conditions can be written as

$$\rho^2 = \frac{\gamma_2 - \beta_1}{\gamma_1 - \beta_2} = \frac{\delta_1}{\delta_2} = \frac{\mu_1}{\mu_2}, \qquad \gamma_1 \neq \beta_2. \tag{8}$$

Moreover, the common ratio in (8) must be positive because ρ is real and nonzero. The equalities in (8) define the coefficient manifold on which the locked vector state can persist. The first ratio balances the effective self-phase and cross-phase modulation of the two components, whereas the second and third ratios match their two nonlinear-dispersive responses. Outside this manifold, the components generally accumulate unequal nonlinear phase shifts or experience unequal dispersive deformation, so a constant amplitude ratio cannot be maintained. Under these conditions, the coupled system reduces to

$$iq_t + \alpha q_{xx} + B|q|^2 q + C_1|q|^2 q_{xx} + C_2\left(|q|^2\right)_{xx} q = 0, \tag{9}$$

where

$$B = \beta_1 + \gamma_1\rho^2 = \gamma_2 + \beta_2\rho^2, \qquad C_1 = \delta_1 = \delta_2\rho^2, \qquad C_2 = \mu_1 = \mu_2\rho^2. \tag{10}$$

For the real-profile traveling-wave reduction, we use

$$q(x,t) = \Phi(\xi)\exp\left[i\left(-\kappa x + \omega t + \theta_0\right)\right], \qquad \xi = x - vt,$$

Here x is the spatial coordinate, and t is the evolution variable; $\xi = x - vt$ is the comoving coordinate; $v \in \mathbb{R}$ is the envelope velocity; $\Phi(\xi) \in \mathbb{R}$ is the real envelope profile; $\kappa \in \mathbb{R}$ is the spatial phase slope (carrier wavenumber); $\omega \in \mathbb{R}$ is the temporal phase frequency; $\theta_0 \in \mathbb{R}$ is an arbitrary constant phase; and $i = \sqrt{-1}$. A prime denotes differentiation with respect to ξ, namely $\Phi' = d\Phi / d\xi$ and $\Phi'' = d^2\Phi / d\xi^2$. Substitution of (11) into (9), followed by separation into real and imaginary parts, gives

$$\left(B - C_1\kappa^2\right)\Phi^3 - \left(\alpha\kappa^2 + \omega\right)\Phi + 2C_2\Phi(\Phi')^2 + \alpha\Phi'' + C_1\Phi^2\Phi'' + 2C_2\Phi^2\Phi'' = 0, \tag{12}$$

and

$$-\left(v + 2\alpha\kappa + 2C_1\kappa\Phi^2\right)\Phi' = 0. \tag{13}$$

For a nonconstant localized real profile, $\Phi' \not\equiv 0$ and Φ^2 is not constant. The notation $\Phi' \not\equiv 0$ means that Φ' is not identically zero on its domain; it may still vanish at isolated points. The symbol $\not\equiv$ denotes “not identically equal to” and is unrelated to the integer set $\mathbb{Z}$. Hence, when $C_1 \neq 0$, Eq. (13) cannot hold for all ξ unless

$$\kappa = 0, \qquad v = 0. \tag{14}$$

Thus, within the proportional real-profile ansatz (11), with a common constant amplitude ratio and a common linear carrier phase, the admissible nonconstant localized waves are quiescent. This statement is conditional on the adopted reduction and is not a global nonexistence result for traveling solutions of the original coupled system. More general complex or chirped profiles, component-dependent phases, a constant complex amplitude ratio, spatially varying amplitude ratios, or nonproportional envelopes may admit localized waves with nonzero velocity. The corresponding two-component quiescent form is

$$\begin{pmatrix} q(x,t) \\ r(x,t) \end{pmatrix} = \begin{pmatrix} 1 \\ \rho \end{pmatrix} \Phi(x)\exp\left[i\left(\omega t + \theta_0\right)\right]. \tag{15}$$

Accordingly, (12) reduces to

$$\left[\alpha + \left(C_1 + 2C_2\right)\Phi^2\right]\Phi'' + 2C_2\Phi(\Phi')^2 + B\Phi^3 - \omega\Phi = 0. \tag{16}$$

For $\alpha \neq 0$, this equation becomes

$$\left(1+\sigma_1\Phi^2\right)\Phi''+\sigma_2\Phi(\Phi')^2+\sigma_3\Phi^3+\sigma_4\Phi=0, \tag{17}$$

where

$$\sigma_1=\frac{C_1+2C_2}{\alpha}, \quad \sigma_2=\frac{2C_2}{\alpha}, \quad \sigma_3=\frac{B}{\alpha}, \quad \sigma_4=-\frac{\omega}{\alpha}. \tag{18}$$

Eq. (17) is now the normalized stationary profile equation for the real envelope $\Phi(x)$. Therefore, the construction of proportional vector quiescent solitons is reduced to solving this nonlinear ordinary differential equation under the compatibility conditions (7)–(8). In the next section, the enhanced direct algebraic method is applied to obtain explicit closed-form profiles.

3. Enhanced direct algebraic construction

In this section, we construct explicit solutions of the quiescent profile equation (17) by applying the enhanced direct algebraic method. The method represents the real profile $\Phi(x)$ as a finite polynomial in an auxiliary function $\Theta(x)$, whose derivative satisfies a quartic polynomial relation. Accordingly, we use the finite expansion

$$\Phi(x)=\mathcal{A}_0+\sum_{j=1}^{N}\mathcal{A}_j\Theta^j(x), \tag{19}$$

where $\mathcal{A}_j$ are constants and $\Theta(x)$ satisfies

$$\left(\Theta'(x)\right)^2=\sum_{\ell=0}^{4}\lambda_\ell\Theta^\ell(x), \quad \lambda_4\neq 0. \tag{20}$$

Differentiating (20) gives

$$\Theta''(x)=\frac{1}{2}\left(\lambda_1+2\lambda_2\Theta+3\lambda_3\Theta^2+4\lambda_4\Theta^3\right). \tag{21}$$

Balancing the linear second-derivative term with the algebraic cubic term in (17) gives $N+2=3N$, and hence $N=1$. The nonlinear derivative terms generate additional higher-order powers, whose leading coefficient subsequently yields the closure condition $2\sigma_1+\sigma_2=0$. Therefore,

$$\Phi(x)=\mathcal{A}_0+\mathcal{A}_1\Theta(x), \quad \mathcal{A}_1\neq 0. \tag{22}$$

Substitution of (22) together with (21) into (17), followed by equating coefficients of powers of Θ, gives the algebraic system

$$\mathcal{E}_5=\left(2\sigma_1+\sigma_2\right)\mathcal{A}_1^3\lambda_4=0, \tag{23}$$

$$\mathcal{E}_4=4\sigma_1\mathcal{A}_0\mathcal{A}_1^2\lambda_4+\frac{3}{2}\sigma_1\mathcal{A}_1^3\lambda_3+\sigma_2\mathcal{A}_0\mathcal{A}_1^2\lambda_4+\sigma_2\mathcal{A}_1^3\lambda_3=0, \tag{24}$$

$$\begin{aligned}\mathcal{E}_3=&\,2\sigma_1\mathcal{A}_0^2\mathcal{A}_1\lambda_4+3\sigma_1\mathcal{A}_0\mathcal{A}_1^2\lambda_3+\sigma_1\mathcal{A}_1^3\lambda_2\\&+\sigma_2\mathcal{A}_0\mathcal{A}_1^2\lambda_3+\sigma_2\mathcal{A}_1^3\lambda_2+\sigma_3\mathcal{A}_1^3+2\mathcal{A}_1\lambda_4=0,\end{aligned} \tag{25}$$

$$\begin{aligned}\mathcal{E}_2=&\,\frac{3}{2}\sigma_1\mathcal{A}_0^2\mathcal{A}_1\lambda_3+2\sigma_1\mathcal{A}_0\mathcal{A}_1^2\lambda_2+\frac{1}{2}\sigma_1\mathcal{A}_1^3\lambda_1\\&+\sigma_2\mathcal{A}_0\mathcal{A}_1^2\lambda_2+\sigma_2\mathcal{A}_1^3\lambda_1+3\sigma_3\mathcal{A}_0\mathcal{A}_1^2+\frac{3}{2}\mathcal{A}_1\lambda_3=0,\end{aligned} \tag{26}$$

$$\mathcal{E}_1 = \sigma_1 \mathcal{A}_0^2 \mathcal{A}_1 \lambda_2 + \sigma_1 \mathcal{A}_0 \mathcal{A}_1^2 \lambda_1 + \sigma_2 \mathcal{A}_0 \mathcal{A}_1^2 \lambda_1 + \sigma_2 \mathcal{A}_1^3 \lambda_0 + 3\sigma_3 \mathcal{A}_0^2 \mathcal{A}_1 + \sigma_4 \mathcal{A}_1 + \mathcal{A}_1 \lambda_2 = 0, \tag{27}$$

$$\mathcal{E}_0 = \frac{1}{2}\sigma_1 \mathcal{A}_0^2 \mathcal{A}_1 \lambda_1 + \sigma_2 \mathcal{A}_0 \mathcal{A}_1^2 \lambda_0 + \sigma_3 \mathcal{A}_0^3 + \sigma_4 \mathcal{A}_0 + \frac{1}{2}\mathcal{A}_1 \lambda_1 = 0. \tag{28}$$

Because $\mathcal{A}_1 \neq 0$ and $\lambda_4 \neq 0$, Eq. (23) requires

$$2\sigma_1 + \sigma_2 = 0. \tag{29}$$

Using (18), this condition becomes

$$C_1 + 3C_2 = 0. \tag{30}$$

In terms of the original coupled coefficients, this may be written as

$$\delta_1 + 3\mu_1 = 0, \qquad \delta_2 + 3\mu_2 = 0, \tag{31}$$

provided the proportionality constraints (7) are satisfied. This condition is not a restriction on the definition of the coupled model itself; it is the closure condition for the present polynomial auxiliary-function construction.

Under (29), a principal solution class is obtained by choosing

$$\mathcal{A}_0 = 0, \qquad \lambda_1 = \lambda_3 = 0. \tag{32}$$

The algebraic system then gives

$$\lambda_2 = -\sigma_4 + 2\sigma_1 \mathcal{A}_1^2 \lambda_0, \qquad \lambda_4 = \frac{\mathcal{A}_1^2}{2}(\sigma_1 \lambda_2 - \sigma_3). \tag{33}$$

4. Vector quiescent soliton families

For compactness, define the vector field

$$\mathbf{Q}(x,t) = \begin{pmatrix} q(x,t) \\ r(x,t) \end{pmatrix}. \tag{34}$$

Then every scalar profile $\Phi_j(x)$ generated by (17) produces the proportional vector quiescent solution

$$\mathbf{Q}_j(x,t) = \begin{pmatrix} 1 \\ \rho \end{pmatrix} \Phi_j(x) \exp[i(\omega t + \theta_0)]. \tag{35}$$

The parameter ρ must satisfy (8), while the exact solutions generated by the present ansatz must also satisfy (30).

4.1 .Bright and singular vector quiescent solitons

For the bright and singular family, take

$$\lambda_0 = \lambda_1 = \lambda_3 = 0. \tag{36}$$

Then

$$\lambda_2 = -\sigma_4, \qquad \lambda_4 = -\frac{\mathcal{A}_1^2}{2}(\sigma_3 + \sigma_1 \sigma_4). \tag{37}$$

If

$$\sigma_4 \langle 0, \qquad \sigma_3 + \sigma_1 \sigma_4 \rangle 0, \tag{38}$$

then the bright vector quiescent soliton is

$$\mathbf{Q}_1(x,t) = \pm \begin{pmatrix} 1 \\ \rho \end{pmatrix} \sqrt{-\frac{2\sigma_4}{\sigma_3 + \sigma_1 \sigma_4}} \operatorname{sech}\left(\sqrt{-\sigma_4}\, x\right) \exp[i(\omega t + \theta_0)]. \tag{39}$$

If

$$\sigma_4 < 0, \qquad \sigma_3 + \sigma_1\sigma_4 < 0, \tag{40}$$

then the singular vector quiescent soliton is

$$\mathbf{Q}_2(x,t) = \pm\begin{pmatrix}1\\ \rho\end{pmatrix}\sqrt{\frac{2\sigma_4}{\sigma_3+\sigma_1\sigma_4}}\operatorname{csch}\left(\sqrt{-\sigma_4}\,x\right)\exp\left[i(\omega t+\theta_0)\right]. \tag{41}$$

4.2. Dark and singular kink-type vector quiescent solitons

For the kink-type family, impose

$$\lambda_0 = \frac{\lambda_2^2}{4\lambda_4}, \qquad \lambda_1 = \lambda_3 = 0. \tag{42}$$

The corresponding coefficients are

$$\lambda_2 = \frac{\sigma_3\sigma_4}{\sigma_1\sigma_4-\sigma_3}, \qquad \lambda_4 = \frac{\sigma_3^2\mathcal{A}_1^2}{2(\sigma_1\sigma_4-\sigma_3)}. \tag{43}$$

Thus, the kink-type vector quiescent soliton is

$$\mathbf{Q}_3(x,t) = \pm\begin{pmatrix}1\\ \rho\end{pmatrix}\sqrt{-\frac{\sigma_4}{\sigma_3}}\tanh\left(\sqrt{-\frac{\sigma_3\sigma_4}{2(\sigma_1\sigma_4-\sigma_3)}}\,x\right)\exp\left[i(\omega t+\theta_0)\right]. \tag{44}$$

The associated singular kink-type vector quiescent soliton is

$$\mathbf{Q}_4(x,t) = \pm\begin{pmatrix}1\\ \rho\end{pmatrix}\sqrt{-\frac{\sigma_4}{\sigma_3}}\coth\left(\sqrt{-\frac{\sigma_3\sigma_4}{2(\sigma_1\sigma_4-\sigma_3)}}\,x\right)\exp\left[i(\omega t+\theta_0)\right]. \tag{45}$$

The real-valued condition is

$$\sigma_3\sigma_4\rangle 0, \qquad \sigma_1\sigma_4-\sigma_3\rangle 0. \tag{46}$$

4.3. Jacobi elliptic vector quiescent solutions

Let

$$R = \frac{\lambda_0\lambda_4}{\lambda_2^2}. \tag{47}$$

Using (33), one obtains

$$\lambda_2^{(\pm)} = \frac{\sigma_1\sigma_4-\sigma_3\pm\Lambda_R}{2\sigma_1(4R-1)}, \tag{48}$$

and

$$\lambda_4^{(\pm)} = \frac{\mathcal{A}_1^2\left[\sigma_1\sigma_4-8R\sigma_3+\sigma_3\pm\Lambda_R\right]}{4(4R-1)}, \tag{49}$$

where

$$\Lambda_R = \sqrt{(\sigma_1\sigma_4+\sigma_3)^2-16R\sigma_1\sigma_3\sigma_4}. \tag{50}$$

For the cn -type solution, take

$$R = \frac{m^2(1-m^2)}{(2m^2-1)^2}, \qquad 2m^2-1\neq 0. \tag{51}$$

Then

$$\mathbf{Q}_5(x,t) = \pm\begin{pmatrix}1\\ \rho\end{pmatrix}\mathcal{A}_1\sqrt{-\frac{m^2\lambda_2^{(\pm)}}{(2m^2-1)\lambda_4^{(\pm)}}}\operatorname{cn}\left(\sqrt{\frac{\lambda_2^{(\pm)}}{2m^2-1}}\,x\,|\,m\right)\exp\left[i(\omega t+\theta_0)\right]. \tag{52}$$

For the dn-type solution, choose

$$R=\frac{1-m^2}{(2-m^2)^2},\qquad 2-m^2\neq 0. \tag{53}$$

Then

$$\mathbf{Q}_6(x,t)=\pm\begin{pmatrix}1\\ \rho\end{pmatrix}\mathcal{A}_1\sqrt{-\frac{m^2\lambda_2^{(\pm)}}{(2-m^2)\lambda_4^{(\pm)}}}\,\mathrm{dn}\left(\sqrt{\frac{\lambda_2^{(\pm)}}{2-m^2}}\,x\mid m\right)\exp\left[i(\omega t+\theta_0)\right]. \tag{54}$$

For the sn -type solution, take

$$R=\frac{m^2}{(m^2+1)^2}. \tag{55}$$

Then

$$\mathbf{Q}_7(x,t)=\pm\begin{pmatrix}1\\ \rho\end{pmatrix}\mathcal{A}_1\sqrt{-\frac{m^2\lambda_2^{(\pm)}}{(m^2+1)\lambda_4^{(\pm)}}}\,\mathrm{sn}\left(\sqrt{-\frac{\lambda_2^{(\pm)}}{m^2+1}}\,x\mid m\right)\exp\left[i(\omega t+\theta_0)\right]. \tag{56}$$

The limiting relations

$$\mathrm{cn}(x\,|\,1)=\mathrm{sech}(x),\qquad \mathrm{dn}(x\,|\,1)=\mathrm{sech}(x),\qquad \mathrm{sn}(x\,|\,1)=\tanh(x) \tag{57}$$

show that (52) and (54) reduce to the bright vector soliton (39), whereas (56) reduces to the kink-type vector soliton (44) in the appropriate nondegenerate limiting sense.

4.4 Weierstrass elliptic vector quiescent solutions

The Weierstrass elliptic solutions follow from

$$\lambda_1=\lambda_3=0,\qquad \lambda_2=-\sigma_4+2\sigma_1\mathcal{A}_1^2\lambda_0,\qquad \lambda_4=\frac{\mathcal{A}_1^2}{2}(\sigma_1\lambda_2-\sigma_3). \tag{58}$$

The invariants are

$$g_2=\frac{\lambda_2^2}{12}+\lambda_0\lambda_4,\qquad g_3=\frac{\lambda_2}{216}\left(36\lambda_0\lambda_4-\lambda_2^2\right). \tag{59}$$

Accordingly,

$$\mathbf{Q}_8(x,t)=\begin{pmatrix}1\\ \rho\end{pmatrix}\mathcal{A}_1\frac{3\wp'(x;g_2,g_3)}{\sqrt{\lambda_4}\left[6\wp(x;g_2,g_3)+\lambda_2\right]}\exp\left[i(\omega t+\theta_0)\right],\qquad \lambda_4>0, \tag{60}$$

and

$$\mathbf{Q}_9(x,t)=\begin{pmatrix}1\\ \rho\end{pmatrix}\mathcal{A}_1\frac{\sqrt{\lambda_0}\left[6\wp(x;g_2,g_3)+\lambda_2\right]}{3\wp'(x;g_2,g_3)}\exp\left[i(\omega t+\theta_0)\right],\qquad \lambda_0>0. \tag{61}$$

The Weierstrass elliptic functions degenerate to hyperbolic functions when

$$g_2^3-27g_3^2=0. \tag{62}$$

For $\lambda_0=0$, Eq. (60) reduces to the singular vector quiescent soliton (41) under the corresponding reality conditions.

4.5. Straddled vector quiescent soliton solutions

For the straddled family, set

$$\lambda_0=\lambda_1=0. \tag{63}$$

A nonzero-background solution is obtained when

$$\mathcal{A}_0^2=-\frac{\sigma_4}{\sigma_3}, \tag{64}$$

and

$$\lambda_2 = -\frac{2\sigma_3\sigma_4}{\sigma_1\sigma_4-\sigma_3}, \qquad \lambda_4 = \frac{\sigma_3^2\mathcal{A}_1^2}{2(\sigma_1\sigma_4-\sigma_3)}, \qquad \lambda_3 = \frac{4\mathcal{A}_0\lambda_4}{\mathcal{A}_1}. \tag{65}$$

Thus,

$$\mathbf{Q}_{10}(x,t) = \begin{pmatrix}1\\ \rho\end{pmatrix}\left[\mathcal{A}_0 + \mathcal{A}_1\frac{-\lambda_2 sech^2\left(\frac{1}{2}\sqrt{\lambda_2}x\right)}{\pm2\sqrt{\lambda_2\lambda_4}\tanh\left(\frac{1}{2}\sqrt{\lambda_2}x\right)+\lambda_3}\right]\exp\left[i(\omega t+\theta_0)\right], \tag{66}$$

and

$$\mathbf{Q}_{11}(x,t) = \begin{pmatrix}1\\ \rho\end{pmatrix}\left[\mathcal{A}_0 + \mathcal{A}_1\frac{\lambda_2 csch^2\left(\frac{1}{2}\sqrt{\lambda_2}x\right)}{\pm2\sqrt{\lambda_2\lambda_4}\coth\left(\frac{1}{2}\sqrt{\lambda_2}x\right)+\lambda_3}\right]\exp\left[i(\omega t+\theta_0)\right]. \tag{67}$$

For $\lambda_3 \neq 0$, another straddled pair is

$$\mathbf{Q}_{12}(x,t) = \begin{pmatrix}1\\ \rho\end{pmatrix}\left[\mathcal{A}_0 - \mathcal{A}_1\frac{\lambda_2\lambda_3 sech^2\left(\frac{\sqrt{\lambda_2}}{2}x\right)}{\lambda_3^2-\lambda_2\lambda_4\left[1-\tanh\left(\frac{\sqrt{\lambda_2}}{2}x\right)\right]^2}\right]\exp\left[i(\omega t+\theta_0)\right], \tag{68}$$

and

$$\mathbf{Q}_{13}(x,t) = \begin{pmatrix}1\\ \rho\end{pmatrix}\left[\mathcal{A}_0 + \mathcal{A}_1\frac{\lambda_2\lambda_3 csch^2\left(\frac{\sqrt{\lambda_2}}{2}x\right)}{\lambda_3^2-\lambda_2\lambda_4\left[1-\coth\left(\frac{\sqrt{\lambda_2}}{2}x\right)\right]^2}\right]\exp\left[i(\omega t+\theta_0)\right]. \tag{69}$$

The straddled solutions reduce to the standard kink-type vector solutions under suitable parameter restrictions. In particular,

$$\begin{aligned}\mathcal{A}_0^2 &= \frac{\mathcal{A}_1^2\lambda_2}{4\lambda_4},\\ \lambda_3 &= \pm2\sqrt{\lambda_2\lambda_4}.\end{aligned} \tag{70}$$

With a consistent sign choice, (66) reduces to (44), while (67) reduces to (45).

5. Discussion and validation of the exact solutions

The solution families obtained above are connected through several limiting processes. These limiting relations show that the elliptic, Weierstrass, and straddled forms are broader solution classes that contain elementary hyperbolic solitons as special cases. They also provide a consistency check on the algebraic construction.

First, the Jacobi elliptic families reduce to hyperbolic profiles when the elliptic modulus approaches one. In this limit,

$$\begin{aligned}\mathrm{cn}(X\,|\,1) &= \mathrm{sech}(X),\\ \mathrm{dn}(X\,|\,1) &= \mathrm{sech}(X),\\ \mathrm{sn}(X\,|\,1) &= \tanh(X).\end{aligned} \tag{71}$$

Consequently, the cn -type and dn -type vector solutions (52) and (54) degenerate into the bright vector quiescent soliton (39), provided the amplitude and width parameters are identified through (48)–(49). Similarly, the sn -type solution (56) degenerates into the kink-type vector quiescent soliton (44). Thus, the elementary bright and kink-type solitons can be viewed as limiting members of the periodic Jacobi elliptic families.

Second, the Weierstrass elliptic solutions reduce to elementary hyperbolic or singular profiles when the elliptic curve becomes degenerate. This occurs when the discriminant vanishes,

$$g_2^3 - 27g_3^2 = 0. \tag{72}$$

Under this condition, the doubly periodic function $\wp(x; g_2, g_3)$ collapses to a simply periodic or hyperbolic form. In particular, when $\lambda_0 = 0$ and the associated sign restrictions are imposed, (60) reduces to the singular vector quiescent solution (41). Other degenerations are obtained by choosing the repeated root of the Weierstrass cubic consistently with the real-valued conditions of the corresponding hyperbolic profile.

Third, the straddled solutions contain the dark and singular kink-type profiles as special cases. When

$$\begin{gathered}\mathcal{A}_0^2 = \frac{\mathcal{A}_1^2 \lambda_2}{4\lambda_4}, \\ \lambda_3 = \pm 2\sqrt{\lambda_2 \lambda_4},\end{gathered} \tag{73}$$

and the sign in the denominator is chosen consistently, the rational-hyperbolic expression (66) reduces to the standard kink-type vector solution (44). Under the same admissible reduction, the singular straddled expression (67) reduces to the singular kink-type solution (45). These reductions confirm that the straddled family extends the kink-type branch rather than representing an unrelated solution class.

Finally, the scalar limit of the vector family is recovered by fixing the proportionality parameter ρ and considering a single component of (35). If $r = \rho q$ is suppressed after the compatibility conditions have been enforced, the remaining component satisfies the scalar nonlinear dispersive equation (9). Therefore, the vector solutions are genuine proportional extensions of scalar quiescent profiles, with the vector amplitude ratio determined by (8).

5.1 Physical interpretation

The obtained solutions describe proportional vector quiescent structures. Both components have the same spatial profile and phase, while the relative amplitude is fixed by ρ. Thus, the vector character of the solution is carried by the constant polarization-like vector $(1, \rho)^{\mathrm{T}}$. The proportionality parameter is not arbitrary; it is determined by the balance between self-phase modulation, cross-phase modulation, and the two nonlinear dispersive mechanisms through (8).

For finite-power bright states, the locked ratio also fixes the distribution of optical power between the two components. If $P_q = \int_{-\infty}^{\infty} |q|^2 dx$ and $P_r = \int_{-\infty}^{\infty} |r|^2 dx$, then $P_r = \rho^2 P_q$ and $P_{\text{tot}} = (1 + \rho^2) P_q$. Thus, the algebraic compatibility conditions determine not only mathematical consistency but also the modal or polarization power partition. For nonzero-background kink-type states, the same ratio applies to the asymptotic background intensities.

The polarization-locked interpretation is the most direct one when q and r denote orthogonal polarization components with negligible walk-off. A matched-mode interpretation is also possible. By contrast, because the present model has no explicit linear inter-core exchange, the proportional state should not be identified with arbitrary dual-core dynamics; it corresponds only to a locked supermode description when such a reduction is physically justified.

Within the proportional real-profile reduction considered here, nonlinear dispersion produces the quiescent restriction. In the imaginary part of the reduced amplitude system, the term proportional to $C_1\kappa\Phi^2\Phi'$ obstructs ordinary mobile localized waves. Since Φ^2 is not constant for a nonconstant localized profile, the condition can hold for all x only when $\kappa=0$ and $\nu=0$. Consequently, the spatial envelope is pinned, and the temporal dependence appears only through the phase factor.

The term "pinned" is used here in the reduced kinematic sense: the envelope is stationary in the chosen frame because the imaginary-part compatibility condition forces $\nu=0$ for this ansatz. It does not imply material pinning by an external potential, nor does it rule out moving localized states outside the proportional real-profile class.

The effective parameters (18) show how the coupled model controls the stationary profile. The parameter σ_3 contains the effective Kerr contribution $B=\beta_1+\gamma_1\rho^2=\gamma_2+\beta_2\rho^2$, which combines self-phase and cross-phase modulation. The parameters σ_1 and σ_2 contain the effective nonlinear dispersive coefficients C_1 and C_2. Therefore, the amplitude, width, and existence conditions of the vector solitons depend simultaneously on Kerr coupling, cross-phase modulation, frequency detuning, and nonlinear dispersion.

The bright solution represents a two-component localized intensity hump on a zero background. The kink-type amplitude connects two nonzero asymptotic states, while its intensity produces a stationary dark-notch profile. The singular solutions are exact mathematical solutions but contain spatial singularities; hence, they should be interpreted as limiting or idealized structures rather than globally regular optical pulses. The Jacobi and Weierstrass families extend the hyperbolic profiles to periodic and doubly periodic vector structures, while the straddled solutions provide rational-hyperbolic forms that reduce to the standard kink-type profiles under admissible parameter restrictions.

5.2. Validation of the exact solutions

This subsection verifies analytical exactness through four complementary steps: consistency of the proportional vector reduction, satisfaction of the stationary profile equation, direct verification of the elementary hyperbolic branches, and auxiliary-equation verification of the elliptic and straddled branches. Vanishing residuals establish that the formulas solve the governing equations under the stated constraints; they do not establish spectral, orbital, or nonlinear stability.

First, the proportional reduction (3) is valid only under the algebraic constraints (7), or equivalently (8). Under these relations, the two scalar branches (5) and (6) have identical nonlinear coefficients. Hence, any solution $q(x,t)$ of the reduced scalar Eq. (9) automatically generates the vector solution

$$\left(q(x,t),r(x,t)\right)=\left(q(x,t),\rho q(x,t)\right) \tag{74}$$

of the full coupled system (1)–(2). This proves that the proportional vector ansatz introduces no additional residual term.

Second, the quiescent substitution (15) converts the reduced scalar equation into the stationary profile Eq. (16), or equivalently into the normalized form (17). Thus, it is sufficient to check that each scalar profile $\Phi_j(x)$ satisfies (17). For the enhanced direct algebraic ansatz (22), the auxiliary equation (20) and its derivative (21) give

$$\begin{aligned} &\Phi' = \mathcal{A}_1\Theta', \\ &\Phi'' = \frac{\mathcal{A}_1}{2}\left(\lambda_1 + 2\lambda_2\Theta + 3\lambda_3\Theta^2 + 4\lambda_4\Theta^3\right). \end{aligned} \tag{75}$$

Substitution of (22) and (75) into (17) yields the polynomial identity

$$\sum_{j=0}^{5}\mathcal{E}_j\Theta^j = 0. \tag{76}$$

The coefficients $\mathcal{E}_j$ are exactly the algebraic quantities displayed in Section 3. Therefore, whenever the algebraic relations (29), (32), and (33) are imposed, all coefficients in (76) vanish. This proves that the generated scalar profiles solve the normalized profile equation.

Third, the elementary hyperbolic solutions can be verified directly. For the bright branch (39), let

$$\begin{aligned} &\Phi(x) = A\operatorname{sech}(kx), \\ &A^2 = -\frac{2\sigma_4}{\sigma_3 + \sigma_1\sigma_4}, \\ &k^2 = -\sigma_4. \end{aligned} \tag{77}$$

Using

$$\frac{d^2}{dx^2}\operatorname{sech}(kx) = k^2\operatorname{sech}(kx) - 2k^2\operatorname{sech}^3(kx), \tag{78}$$

and substituting (77) into (17), the coefficients of $\operatorname{sech}(kx)$, $\operatorname{sech}^3(kx)$, and $\operatorname{sech}^5(kx)$ vanish under (29). Hence, the bright vector field (39) is an exact solution. The singular branch (41) follows by the same calculation with $\operatorname{csch}(kx)$ and the corresponding sign condition on $\sigma_3 + \sigma_1\sigma_4$.

For the kink-type branch (44), let

$$\begin{aligned} &\Phi(x) = A\tanh(kx), \\ &A^2 = -\frac{\sigma_4}{\sigma_3}, \\ &k^2 = -\frac{\sigma_3\sigma_4}{2(\sigma_1\sigma_4 - \sigma_3)}. \end{aligned} \tag{79}$$

Using

$$\frac{d^2}{dx^2}\tanh(kx) = -2k^2\tanh(kx)\operatorname{sech}^2(kx), \tag{80}$$

and rewriting $\operatorname{sech}^2(kx) = 1 - \tanh^2(kx)$, substitution into (17) again gives an identity in powers of $\tanh(kx)$. The coefficients vanish under (29) and (79). The singular kink-type solution (45) is validated analogously by using $d(\coth(kx))/dx = -k\operatorname{csch}^2(kx)$.

Fourth, the elliptic and Weierstrass branches are validated by the same auxiliary-equation mechanism. The Jacobi profiles (52)–(56) are obtained from special quartic choices in (20); hence, their substitution reduces to (76). The Weierstrass profiles (60)–(61) satisfy the quartic auxiliary relation after transformation to the Weierstrass equation with invariants g_2 and g_3. Therefore, they also satisfy (17). The straddled profiles (66)–(69) follow from the hyperbolic rational solutions of the same auxiliary equation, so their validation is again a consequence of (76).

It should also be emphasized that the above validation holds subject to the parameter restrictions stated in the construction. In particular, the proportionality constraints (7)–(8), the closure condition (31), the nonzero-denominator assumptions, and the corresponding real-valuedness and regularity conditions are all required. Under these assumptions, the residual of the normalized profile Eq. (17) vanishes identically, and therefore the residuals of the two original coupled Eqs. (1)–(2) vanish through the proportional reduction.

In generating Figs. 1–4, the remaining coefficients are adjusted simultaneously so that the proportionality constraints (7)–(8) and the closure condition (31) remain satisfied for every plotted curve.

Finally, the plotted profiles in Figs. 1–4 illustrate representative regular bright and kink-type vector quiescent solutions under variations of the self-phase modulation, cross-phase modulation, and nonlinear dispersive parameters. These plots are not used as a proof of exactness; rather, they provide a graphical consistency check of the analytical formulae and show how the effective parameters influence the amplitude and width of the two-component profiles.

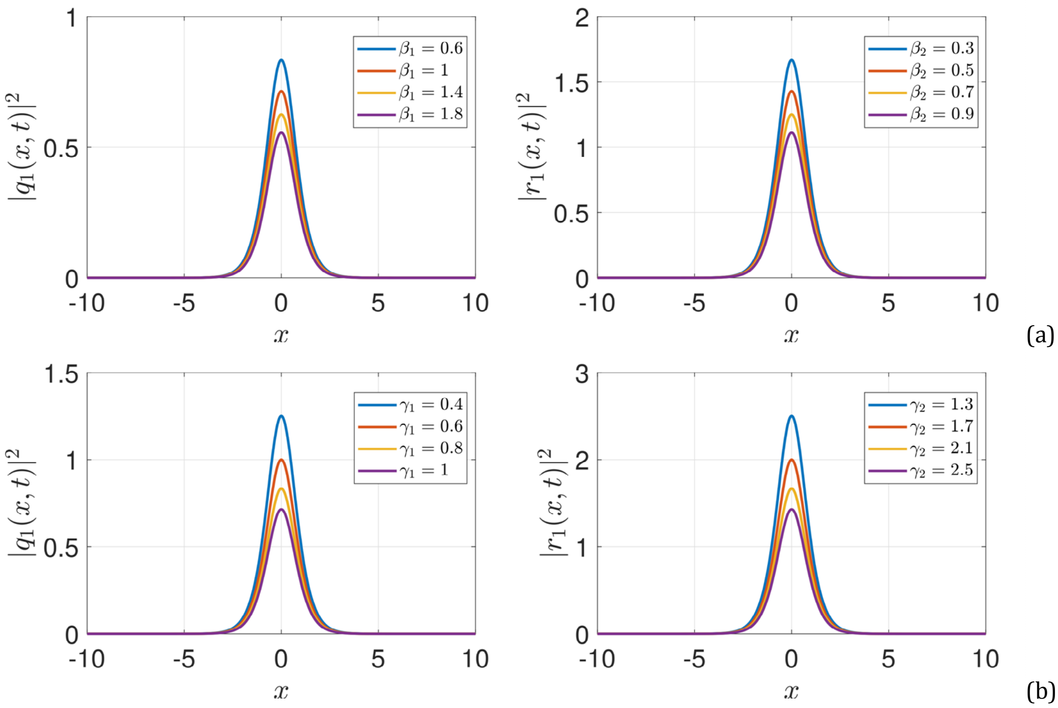

Fig. 1. Intensity profiles of the bright proportional vector quiescent soliton (q_1, r_1) under variations of (β_1, β_2) and (γ_1, γ_2). (a) Variation of the self-phase modulation coefficients β_1 and β_2; (b) Variation of the cross-phase modulation coefficients γ_1 and γ_2.

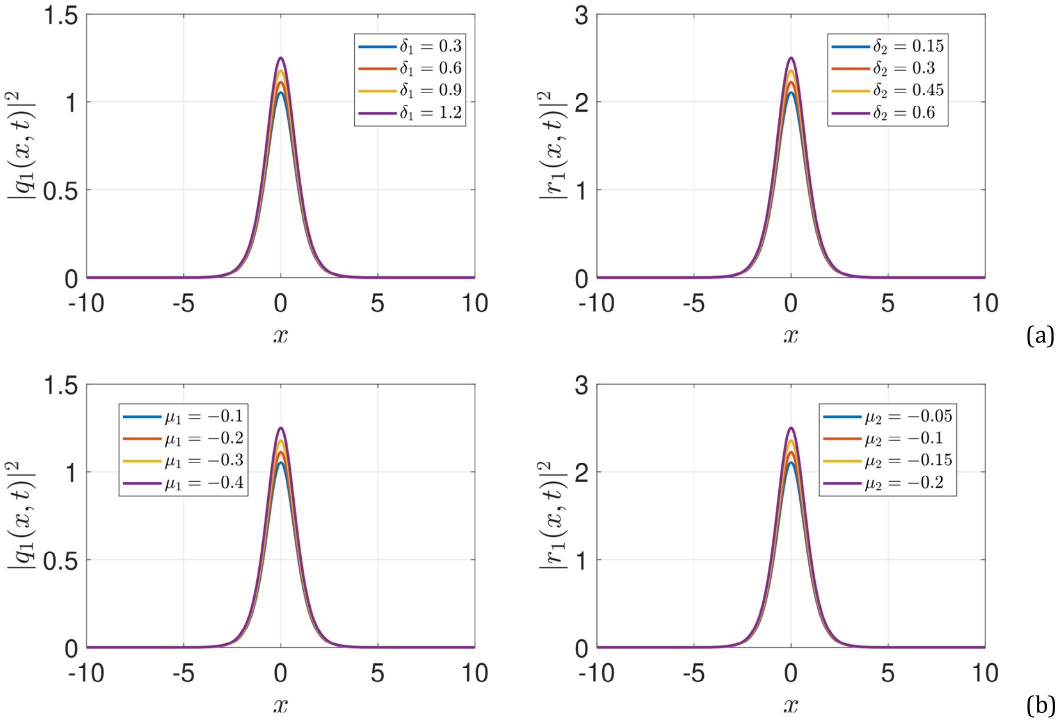

Fig. 2. Intensity profiles of the bright proportional vector quiescent soliton (q_1, r_1) under variations of (δ_1, δ_2) and (μ_1, μ_2). (a) Variation of the nonlinear dispersion coefficients δ_1 and δ_2; (b) Variation of the nonlinear dispersive curvature coefficients μ_1 and μ_2.

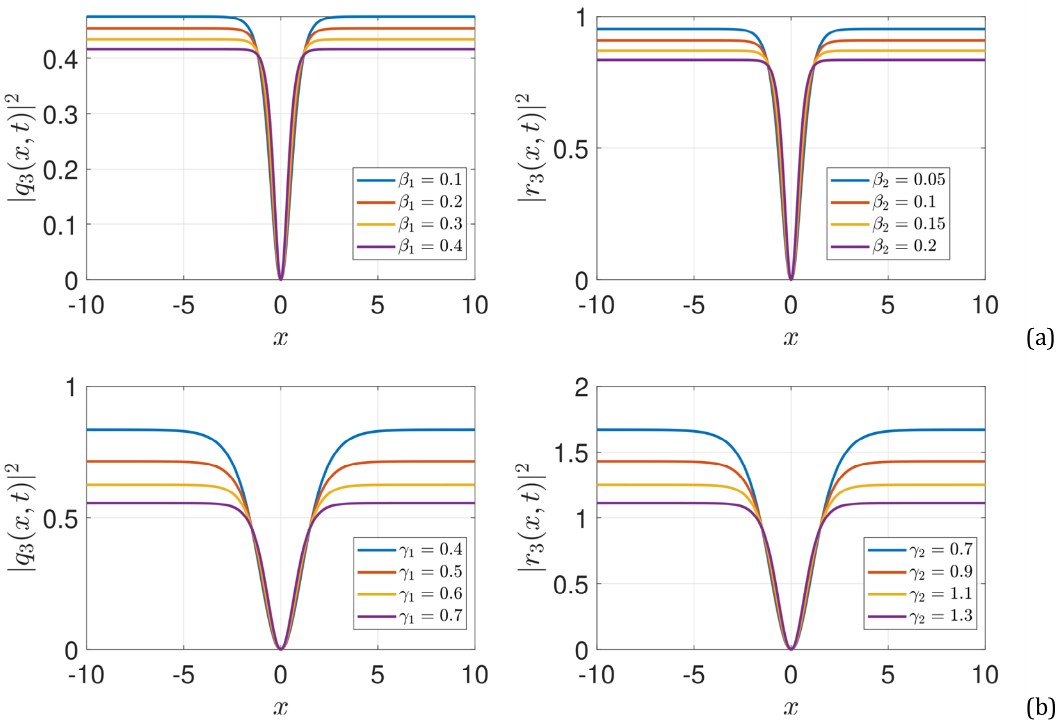

Fig. 3. Intensity profiles of the dark-notch intensity profile associated with the kink-type proportional vector wave (q_3, r_3) under variations of (β_1, β_2) and (γ_1, γ_2). (a) Variation of the self-phase modulation coefficients β_1 and β_2; (b) Variation of the cross-phase modulation coefficients γ_1 and γ_2.

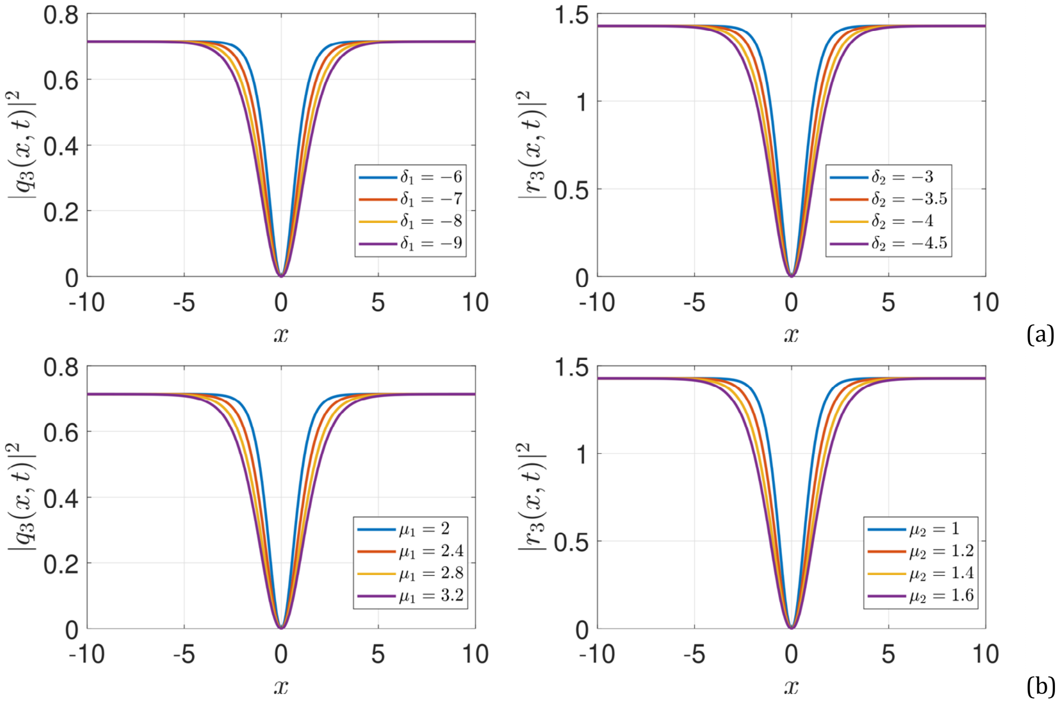

Fig. 4. Intensity profiles of the dark-notch intensity profile associated with the kink-type proportional vector wave (q_3, r_3) under variations of (δ_1, δ_2) and (μ_1, μ_2). (a) Variation of the nonlinear dispersion coefficients δ_1 and δ_2; (b) Variation of the nonlinear dispersive curvature coefficients μ_1 and μ_2.

5.3. Linear spectral stability and direct perturbation robustness

The residual calculations in Section 5.2 prove that the reported profiles are exact solutions, but exactness alone does not determine whether an independently perturbed two-component pulse remains observable. To retain perturbations both tangent and transverse to the proportional manifold, let a regular quiescent profile $\Phi(x)$ be disturbed according to

$$\begin{aligned} q(x,t) &= e^{i(\omega t+\theta_0)}\left[\Phi(x)+\varepsilon\left(u_1(x,t)+iv_1(x,t)\right)\right], \\ r(x,t) &= e^{i(\omega t+\theta_0)}\left[\rho\Phi(x)+\varepsilon\left(u_2(x,t)+iv_2(x,t)\right)\right], \end{aligned} \tag{81}$$

where u_1, v_1, u_2, and v_2 are independent real-valued perturbations and $0<\varepsilon\ll 1$. Enforcing $u_2=\rho u_1$ and $v_2=\rho v_1$ would test only perturbations tangent to $r=\rho q$ and would miss changes of the component ratio and relative phase.

Substitution of (81) into Eqs. (1)–(2), followed by retention of the $O(\varepsilon)$ terms, gives

$$\frac{\partial}{\partial t}\begin{pmatrix} u_1 \\ u_2 \\ v_1 \\ v_2 \end{pmatrix} = \begin{pmatrix} 0 & 0 & -\mathcal{L}_{1-} & 0 \\ 0 & 0 & 0 & -\mathcal{L}_{2-} \\ \mathcal{L}_{1+} & \mathcal{M}_{12} & 0 & 0 \\ \mathcal{M}_{21} & \mathcal{L}_{2+} & 0 & 0 \end{pmatrix}\begin{pmatrix} u_1 \\ u_2 \\ v_1 \\ v_2 \end{pmatrix} \equiv \mathcal{J}\mathbf{w}, \tag{82}$$

where

$$\begin{aligned} \mathcal{L}_{1-}f &= \left(\alpha+\delta_1\Phi^2\right)f_{xx}+\left[-\omega+B\Phi^2+\mu_1(\Phi^2)_{xx}\right]f, \\ \mathcal{L}_{2-}f &= \left(\alpha+\delta_2\rho^2\Phi^2\right)f_{xx}+\left[-\omega+B\Phi^2+\mu_2\rho^2(\Phi^2)_{xx}\right]f, \end{aligned} \tag{83}$$

and

$$
\begin{aligned}
\mathcal{L}_{1+}f &= \left(\alpha+\delta_1\Phi^2\right)f_{xx}+2\mu_1\Phi(\Phi f)_{xx} \\
&\quad+\left[-\omega+\left(3\beta_1+\gamma_1\rho^2\right)\Phi^2+2\delta_1\Phi\Phi_{xx}+\mu_1(\Phi^2)_{xx}\right]f, \\
\mathcal{L}_{2+}f &= \left(\alpha+\delta_2\rho^2\Phi^2\right)f_{xx}+2\mu_2\rho^2\Phi(\Phi f)_{xx} \\
&\quad+\left[-\omega+\left(\gamma_2+3\beta_2\rho^2\right)\Phi^2+2\delta_2\rho^2\Phi\Phi_{xx}+\mu_2\rho^2(\Phi^2)_{xx}\right]f, \\
\mathcal{M}_{12}f &= 2\gamma_1\rho\Phi^2 f, \\
\mathcal{M}_{21}f &= 2\gamma_2\rho\Phi^2 f.
\end{aligned}
\tag{84}
$$

The signs in (82) follow from the real and imaginary parts of $i\left(u_{j,t}+iv_{j,t}\right)$. In particular, $u_{j,t}=-\mathcal{L}_{j-}v_j$, whereas the amplitude operators enter the $v_{j,t}$ equations with positive signs.

With $\mathbf{w}(x,t)=e^{\lambda t}\mathbf{W}(x)$, Eq. (82) becomes

$$\lambda\mathbf{W}=\mathcal{J}\mathbf{W}. \tag{85}$$

Spectral instability occurs when the spectrum contains an eigenvalue with $Re(\lambda)>0$. For a bright state, the problem is posed on $L^2(\mathbb{R})^4$ with decaying perturbations. The nonlinear-dispersive terms alter the principal coefficients; regular spectral evolution therefore requires

$$
\begin{aligned}
&\alpha+\delta_1\Phi^2\neq 0, \\
&\alpha+\delta_2\rho^2\Phi^2\neq 0, \\
&r(x,t)=\exp\left(i\left(\omega t+\theta_0\right)\right)\left[\rho\Phi(x)+\varepsilon\left(u_2(x,t)+iv_2(x,t)\right)\right],
\end{aligned}
\tag{86}
$$

throughout the profile. The first line controls the phase channel, whereas the second line is obtained by expanding the highest-derivative part of $2\mu_jQ_j(Q_jf)_{xx}$ in the amplitude channel.

A representative regular bright state was tested using

$$
\begin{aligned}
&\alpha=1,\quad \omega=1,\quad \rho=\sqrt{2}, \\
&\left(\beta_1,\beta_2,\gamma_1,\gamma_2\right)=\left(0.6,0.3,0.2,0.4\right), \\
&\left(\delta_1,\delta_2\right)=\left(0.3,0.15\right), \\
&\left(\mu_1,\mu_2\right)=\left(-0.1,-0.05\right).
\end{aligned}
\tag{87}
$$

These values satisfy Eqs. (7) and (31), and give $B=1$, $\left(\sigma_1,\sigma_2,\sigma_3,\sigma_4\right)=\left(0.1,-0.2,1,-1\right)$. Hence,

$$
\begin{aligned}
&\Phi_b(x)=\sqrt{\frac{20}{9}}\operatorname{sech}x, \\
&\left(q_b,r_b\right)^T=\left(1,\sqrt{2}\right)^T\Phi_b(x)\exp(it).
\end{aligned}
\tag{88}
$$

For this profile, all four principal coefficients in (86) are strictly positive: the phase coefficients are $1+0.3\Phi_b^2$, and the amplitude coefficients are $1+0.1\Phi_b^2$. Thus, the linearized operator does not lose differential order across the pulse.

As $|x|\to\infty$, $\Phi_b\to 0$ and all diagonal operators approach $\mathcal{L}_\infty=\alpha\partial_x^2-\omega$. A Fourier mode $\exp(i\xi x)$ therefore yields

$$\lambda=\pm i\left(\alpha\xi^2+\omega\right), \tag{89}$$

with multiplicity two. For (87), the essential spectrum is

$$\sigma_{\text{ess}}(\mathcal{J})=i(-\infty,-1]\cup i[1,\infty), \tag{90}$$

which lies entirely on the imaginary axis. The two independent phase symmetries and spatial translation generate the neutral directions $(0,0,\Phi_b,0)^T$, $(0,0,0,\rho\Phi_b)^T$, and $(\Phi_{b'},\rho\Phi_{b'},0,0)^T$ at $\lambda=0$.

The point spectrum was computed by Chebyshev collocation on $[-20,20]$, with homogeneous Dirichlet conditions imposed on the perturbations at the truncated boundaries. Table 1 shows the rightmost computed real part as the number N_c of Chebyshev intervals is increased. The small positive value observed at lower resolution is the familiar numerical splitting of the symmetry-generated zero eigenvalues; it converges to zero. At $N_c=220$, the largest computed real part is 1.46×10^{-11}, and the three neutral pairs lie within 1.47×10^{-5} of the origin. The remaining low-frequency spectrum begins at $|Im\lambda|\simeq0.995$, in agreement with the exact essential-spectrum threshold $|Im\lambda|=1$. Fig. 5 shows the low-frequency spectrum. No eigenvalue with positive real part survives refinement, so the tested bright state is numerically spectrally stable within the stated resolution.

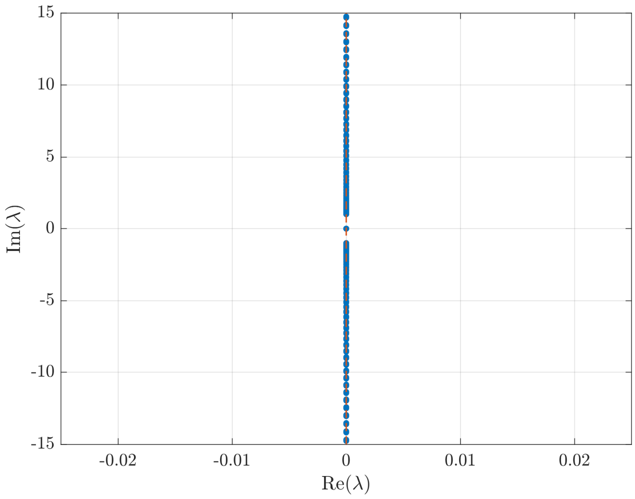

Fig. 5. Low-frequency spectrum of the full four-component linearized operator for the representative bright state (88), computed with $N_C = 220$ Chebyshev intervals on [-20, 20]. The spectrum is confined to the imaginary axis to numerical tolerance; the near-zero points are the phase- and translation-generated neutral modes.

Table 1. Spectral convergence for the representative bright state (88).

N_c	$\max Re(\lambda)$
160	2.56×10^{-3}
180	6.32×10^{-4}
200	1.21×10^{-4}
220	1.46×10^{-11}

To test the nonlinear evolution without preserving $r=\rho q$ by construction, the full coupled PDE system was initialized with independent amplitude and phase disturbances,

$$
\begin{aligned}
q(x,0)&=\Phi_b(x)\left[1+\varepsilon a_q(x)\right]\exp\left(i\varepsilon b_q(x)\right),\\
r(x,0)&=\rho\Phi_b(x)\left[1+\varepsilon a_r(x)\right]\exp\left(i\varepsilon b_r(x)\right),
\end{aligned}
\tag{91}
$$

where $\varepsilon=10^{-2}$ and

$$\begin{aligned} a_q(x) &= 0.8\exp(-(x/4)^2)\cos(0.7x), \\ b_q(x) &= 0.5\exp(-(x/5)^2)\sin(0.9x), \\ a_r(x) &= -0.6\exp(-(x/4.5)^2)\cos(1.1x), \\ b_r(x) &= 0.7\exp(-(x/5)^2)\sin(0.6x). \end{aligned} \tag{92}$$

The unequal functions in the two rows excite both tangent and transverse perturbation channels. The system was integrated on $[-20,20]$ by a Fourier pseudospectral discretization with $N=512$ modes, two-thirds de-aliasing, and fourth-order exponential time differencing with $\Delta t=10^{-3}$ up to $T=20$. Repeating the calculation with $N=256$ and $\Delta t=2\times10^{-3}$ changed the final reported diagnostics by less than 2×10^{-9}.

Because the model is invariant under independent constant phase rotations and spatial translations, robustness was measured after removing these neutral motions. The phase-optimized vector-locking defect and the phase-and-translation-aligned shape errors were defined by

$$\begin{aligned} D_{\text{lock}}(t) &= \min_{\vartheta\in\mathbb{R}} \frac{\|r(\cdot,t)-\rho e^{i\vartheta}q(\cdot,t)\|_2}{\|\rho q(\cdot,t)\|_2}, \\ E_q(t) &= \min_{s,\vartheta\in\mathbb{R}} \frac{\|q(\cdot,t)-e^{i\vartheta}\Phi_b(\cdot-s)\|_2}{\|\Phi_b\|_2}, \\ E_r(t) &= \min_{s,\vartheta\in\mathbb{R}} \frac{\|r(\cdot,t)-\rho e^{i\vartheta}\Phi_b(\cdot-s)\|_2}{\|\rho\Phi_b\|_2}. \end{aligned} \tag{93}$$

Fig. 6 summarizes the quantitative diagnostics from the direct evolution. Over $0\le t\le 20$, the locking defect changes from 1.12×10^{-2} to 1.03×10^{-2}, while $E_q(20)=9.32\times10^{-3}$ and $E_r(20)=7.07\times10^{-3}$. The peak intensities remain in the narrow intervals $2.252\le \max_x|q|^2\le 2.260$ and $4.391\le \max_x|r|^2\le 4.434$. Both components undergo the same small displacement, approximately 0.156, which is consistent with excitation of the neutral translation mode rather than profile breakup. No growing shape deformation or component-unlocking instability is observed over the simulated interval.

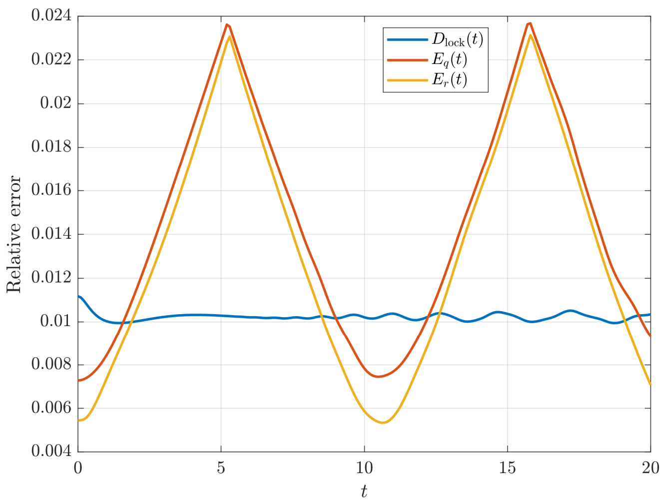

Fig. 6. Phase-optimized vector-locking defect and phase-and-translation-aligned shape errors for the full-system propagation. All diagnostics remain near the one-percent level over the simulated interval.

The combined spectral and direct-evolution evidence therefore supports numerical spectral stability and finite-time perturbation robustness of the representative bright state (88). This conclusion is parameter- and branch-specific: it is not a proof of nonlinear orbital stability for the entire analytical family, and it does not extend to the kink, elliptic, straddled, or singular solutions without separate background, Floquet, or singular-domain analyses.

6. Conclusions

This paper studied proportional vector quiescent solitons in a coupled nonlinear Schrödinger system with Kerr-type self-phase modulation, cross-phase modulation, and nonlinear dispersion. The terminology was kept at the level of nonlinear dispersion in order to emphasize the mathematical structure of the dispersive corrections without linking the model to a narrowly specified material platform. The nonlinear dispersive terms were treated as higher-order corrections that modify the usual balance between dispersion and nonlinearity.

A proportional-amplitude reduction was derived, and the required algebraic compatibility constraints were obtained. These constraints determine the admissible amplitude ratio and connect the self-phase modulation, cross-phase modulation, and nonlinear dispersive coefficients. Under these conditions, the original coupled system reduces consistently to a scalar nonlinear Schrödinger equation with effective nonlinear dispersion. The traveling real-profile reduction then shows that, when the nonlinear dispersive obstruction is active, nonconstant localized waves cannot propagate as ordinary mobile solitons. Instead, the admissible localized real-profile waves are quiescent, with a stationary spatial envelope and a purely temporal phase factor. This conclusion applies only to the common real-profile, constant-ratio, linear-phase ansatz used in the analysis. It does not exclude moving localized waves with chirped or complex profiles, component-dependent phases, or nonproportional vector envelopes.

The resulting stationary profile equation was solved by the enhanced direct algebraic method. Bright, dark kink-type, singular, Jacobi elliptic, Weierstrass elliptic, and straddled proportional vector quiescent soliton families were constructed. The limiting analysis showed that the Jacobi elliptic branches reduce to bright and kink-type hyperbolic solitons, the Weierstrass solutions degenerate to elementary singular or hyperbolic profiles under the appropriate degeneracy condition, and the straddled solutions contain the kink-type solutions as special cases. These limiting relations clarify the hierarchy among the obtained solution families.

An analytical validation of exactness was provided. The proportionality constraints ensure that solutions of the reduced scalar equation solve the original coupled system, while the auxiliary-equation identities and the direct checks of the bright and kink-type branches establish vanishing residuals under the stated parameter restrictions. This validation proves existence and exactness; it is not a stability test. The vector contribution is also not a trivial duplication of a scalar solution, because the two field equations admit a common proportional profile only on the compatibility manifold (8), which fixes the component intensity and power ratio.

The physical robustness question was addressed explicitly for a representative regular bright state. Independent real and imaginary perturbations of the two components produced the full four-component eigenvalue problem (82), including transverse modes that can destroy amplitude and phase locking. The asymptotic dispersion relation placed the essential spectrum on the imaginary axis, and the Chebyshev computation found no point eigenvalue with positive real part after spectral refinement. Direct integration of the full coupled PDEs under independent amplitude and phase perturbations preserved both localized profiles and the vector-locking relation over $0 \le t \le 20$, with phase- and translation-adjusted errors remaining below approximately 1.2%. These results support numerical spectral stability and finite-time robustness of the tested bright branch. They do not constitute a global nonlinear-stability theorem and do not establish stability of the kink, elliptic, straddled, or singular families.

The results provide analytical benchmark solutions for coupled nonlinear dispersive optical models and demonstrate, for one regular parameter set, that the amplitude-locked quiescent state can persist under perturbations of the full vector system. Future work will extend the spectral and direct-evolution calculations to nonzero-background kink states, Floquet perturbations of periodic branches, and nonproportional or chirped vector reductions that may support moving localized waves. Singular branches will remain interpreted as idealized mathematical limits unless an appropriate regularization is introduced.

Disclosure. The authors declare that they have no conflict of interest.

Funding and acknowledgement. This work of the last author (AB) was supported by Grambling State University for the Endowed Chair of Mathematics. The author gratefully acknowledges this support.

Authors contribution: Ahmed H. Arnous: conceptualization, methodology, formal analysis, investigation, visualization, and writing–original draft. Muhammad Amin S. Murad: validation, investigation, and writing–review and editing. Yakup Yildirim: methodology, validation, and writing–review and editing. Oswaldo González–Gaxiola: software, numerical analysis, validation, and writing–review and editing. Anjan Biswas: conceptualization, supervision, project administration, and writing–review and editing. All authors read and approved the final manuscript.

References

1. Ouahid, L., Abdou, M. A., Alshahrani, D. O., & Akgül, A. (2025). New periodic wave solution for time-fractional perturbed nonlinear Schrödinger equation arising in optical fiber via newly extended mapping scheme. *Optical Review, 32*, 608–618.
2. Afridi, M. I., & Hussain, S. (2025). Analyzing multiplicative noise effects on Manakov's model via the new extended direct algebraic method. *Results in Engineering, 27*, 106414.
3. Afridi, M. I., Islam, T., Akbar, M. A., & Osman, M. S. (2024). The investigation of nonlinear time-fractional models in optical fibers and the impact analysis of fractional-order derivatives on solitary waves. *Fractal and Fractional, 8*(11), 627.
4. Asjad, M. I., Sagher, A. A., Riaz, M. B., & Abdallah, S. A. O. (2026). Exploring optical soliton solution for (2+1)-dimensional Kundu–Mukherjee–Naskar equation using two analytical methods with sensitivity analysis. *Journal of the Korean Physical Society, 88*, 352–369.
5. Ilhan, E., Rehman, S. U., Bilal, M., Baskonus, H. M., & Alawaideh, Y. M. (2025). Some novel optical pulses in hydrodynamical nonlinear complex equation using M-truncated fractional derivative. *Scientific Reports, 15*, Article 32139.
6. Jawad, A. J. M., & Abu-AlShaeer, M. J. (2023). Highly dispersive optical solitons with cubic law and cubic-quintic-septic law nonlinearities by two methods. *Al-Rafidain Journal of Engineering Sciences, 1*(1), 1–8.
7. Jihad, N. J., & Almuhsin, M. A. A. (2023). Evaluation of impairment mitigations for optical fiber communications using dispersion compensation techniques. *Al-Rafidain Journal of Engineering Sciences, 1*(1), 81–92.

8. Ma, G., Zhao, J., Zhou, Q., Biswas, A., & Liu, W. (2021). Soliton interaction control through dispersion and nonlinear effects for the fifth-order nonlinear Schrödinger equation. *Nonlinear Dynamics, 106*, 2479–2484.
9. Al Qarni, A. A., Bodaqah, A. M., Mohammed, A. S. H. F., Alshaery, A. A., Bakodah, H. O., & Biswas, A. (2023). Dark and singular cubic–quartic optical solitons with Lakshmanan–Porsezian–Daniel equation by the improved Adomian decomposition scheme. *Ukrainian Journal of Physical Optics, 24*(1), 46–61.
10. Zayed, E. M. E., Alngar, M. E. M., Shohib, R. M. A., Biswas, A., Yıldırım, Y., Moraru, L., Moldovanu, S., & Georgescu, P. L. (2023). Dispersive optical solitons with differential group delay having multiplicative white noise by Itô calculus. *Electronics, 12*, 634.
11. Arnous, A. H., Biswas, A., Kara, A. H., Yıldırım, Y., Moraru, L., Moldovanu, S., Georgescu, P. L., & Alghamdi, A. A. (2023). Dispersive optical solitons and conservation laws of Radhakrishnan–Kundu–Lakshmanan equation with dual–power law nonlinearity. *Heliyon, 9*, Article e14036.
12. Ankiewicz, A., Devine, N., Akhmediev, N., & Soto-Crespo, J. M. (2007). Dissipative solitons and antisolitons. *Physics Letters A, 370*(5–6), 454–459.
13. Ankiewicz, A., Akhmediev, N., & Devine, N. (2006). Two types of stationary solitons in dissipative systems. *Proceedings of ACOFT 2006*, 143–145.
14. Arnous, A. H., Biswas, A., Yildirim, Y., Moraru, L., Moldovanu, S., Iticescu, C., Khan, S., & Alshehri, H. M. (2023). Quiescent optical solitons with quadratic–cubic and generalized quadratic–cubic nonlinearities. *Telecom, 4*(1), 31–42.
15. Ekici, M. (2022). Stationary optical solitons with complex Ginzburg–Landau equation having nonlinear chromatic dispersion and Kudryashov's refractive index structures. *Physics Letters A, 440*, 128146.
16. Anam, N., & Atai, J. (2023). Quiescent solitary waves in dual-core systems with separated Bragg grating and cubic–quintic nonlinearity. *Optik, 287*, 171104.
17. Ekici, M. (2022). Optical solitons with Kudryashov's quintuple power–law coupled with dual form of non-local law of refractive index with extended Jacobi's elliptic function. *Optical and Quantum Electronics, 54*(5), 279.
18. Ekici, M. (2023). Stationary optical solitons with Kudryashov's quintuple power law nonlinearity by extended Jacobi's elliptic function expansion. *Journal of Nonlinear Optical Physics and Materials, 32*(1), 2350008.
19. Han, T., Li, Z., Li, C., & Zhao, L. (2023). Bifurcations, stationary optical solitons and exact solutions for complex Ginzburg–Landau equation with nonlinear chromatic dispersion in non–Kerr law media. *Journal of Optics, 52*, 831–844.
20. Kudryashov, N. A. (2022). Stationary solitons of the generalized nonlinear Schrödinger equation with nonlinear dispersion and arbitrary refractive index. *Applied Mathematics Letters, 128*, 107888.
21. Kudryashov, N. A. (2024). Stationary solitons of the model with nonlinear chromatic dispersion and arbitrary refractive index. *Optik, 259*, 168888.
22. Kuetche Saadeu, G., & Nana, L. (2021). Higher-order spectral filtering effects on the dynamics of stationary soliton in dissipative systems in the presence of linear and nonlinear gain/loss. *Nonlinear Dynamics, 105*, 2559–2573.
23. Akter, A., Islam, M. J., & Atai, J. (2021). Quiescent gap solitons in coupled nonuniform Bragg gratings with cubic–quintic nonlinearity. *Applied Sciences, 11*(11), 4833.
24. Chou, D., Amer, A., Rehman, H. U., & Li, M.-L. (2025). Unravelling quiescent optical solitons: An exploration of the complex Ginzburg–Landau equation with nonlinear chromatic dispersion and self-phase modulation. *Nonlinear Engineering, 14*, 20240043.

Arnous, A.H., Murad, M.A.S., Yildirim, Y., Biswas, A. (2026). Quiescent Vector Optical Solitons with Nonlinear Dispersion. Ukrainian Journal of Physical Optics, 27(4), 04054 – 04076.
doi: 0.3116/16091833/Ukr.J.Phys.Opt.2026.04054

Анотація. *У цій статті досліджуються пропорційні векторні стаціонарні солітони для зв'язаної системи нелінійних рівнянь Шредінгера з самофазовою модуляцією Керрівського типу, крос-фазовою модуляцією та нелінійною дисперсією. Пропорційно-амплітудне редукування вводиться, припускаючи, що дві компоненти мають спільну обвідну та фазу, тоді як їхня відносна амплітуда залишається фіксованою. Фізично це редукування відповідає амплітудно- та фазово-синхронізованому векторному режиму з фіксованим співвідношенням інтенсивностей компонентів. Редукування допустиме лише тоді, коли явні алгебраїчні співвідношення сумісності пов'язують самофазову модуляцію, крос-фазову модуляцію та коефіцієнти нелінійної дисперсії. За цих обмежень зв'язана модель зводиться до скалярного нелінійного рівняння Шредінгера з ефективною нелінійною дисперсією. У рамках пропорційного редукування з дійсним профілем нелінійна дисперсійна структура виключає локалізовані хвилі з ненульовою швидкістю та допускає лише стаціонарні* *профілі. Цей висновок про нульову швидкість обмежений загальним анзацем з дійсним профілем, постійним співвідношенням, лінійною фазою та не виключає рухомі хвилі з більш загальними складними або непропорційними структурами. Отримане стаціонарне рівняння профілю розв'язується вдосконаленим методом прямої алгебри. Отримано точні пропорційні сімейства векторних спокійних хвиль, включаючи яскраві, кінкоподібні, сингулярні, еліптичні хвилі Якобі, еліптичні хвилі Вейєрштрасса та розтягнуті розв'язки. Граничні переходи між цими сімействами та пряма перевірка побудованих профілів підтверджують узгодженість аналітичних результатів. Також отримано повний чотирикомпонентний оператор збурень. Для репрезентативного регулярного яскравого стану спектральний метод Чебишева розміщує спектр на уявній осі з числовою допуском, тоді як пряме моделювання методом Фур'є-ETDRK4 під впливом незалежних компонентних збурень зберігає локалізовану форму та синхронізацію вектора протягом модельованого інтервалу. Ці тести підтверджують числову спектральну стабільність та стійкість у скінченному діапазоні часу лише для протестованої яскравої гілки.*

Ключові слова: *векторні стаціонарні солітони, зв'язана нелінійна система Шредінгера, нелінійна дисперсія, стаціонарна редукція, спектральна стійкість, стійкість до збурень*